EULER FLOW SOLUTIONS FOR A TRANSONIC WIND TUNNEL SECTION

by Barry Koren
Centre for Mathematics and Computer Science
Amsterdam, THE NETHERLANDS

ABSTRACT: Steady, 2D Euler flow computations have been performed for a wind tunnel section, designed for research on transonic shock wave - boundary layer interaction. For the discretization of the steady Euler equations, an upwind finite volume technique has been applied. The solution method used is collective, symmetric point Gauss-Seidel relaxation, accelerated by nonlinear multigrid. Initial finest grid solutions have been obtained by nested iteration. Automatic grid adaptation has been applied for obtaining sharp shocks. An indication is given of the mathematical quality of four different boundary conditions for the outlet flow. Two transonic flow solutions with shock are presented; a choked and a non-choked flow. Both flow solutions show a good shock capturing. A comparison is made with results obtained by holographic interferometry.

DESCRIPTORS: steady Euler equations - transonic flows - multigrid methods - grid generation and adaptation - boundary conditions.

I. INTRODUCTION

An important physical feature for the design of transonic airfoils is the interaction between the possible shock wave(s) at the airfoil and the boundary layers along the airfoil. In transonic aerodynamics a lot of work, both experimental and theoretical, is devoted to this so-called transonic shock wave - boundary layer interaction. At the Delft University of Technology, Faculty of Aerospace Engineering, a transonic wind tunnel section has been designed and constructed [1] for performing measurements on this phenomenon [2]. Limited accessibility to the flow in the wind tunnel section inhibits measurements throughout the entire flow field. However, knowledge of the entire flow field is important for re-design purposes. This situation motivated a computation of the entire flow field.

As a suitable flow model has been chosen: the steady, 2D Euler equations. The Euler equations have been chosen because (in the first instance) only inviscid flow solutions with (possibly occurring) rotation are of interest. The use of a steady flow model is motivated by the fact that the main flow in the wind tunnel section is steady. Further, the use of a 2D flow model is motivated by the fact that the wind tunnel section has a curved lower and upper wall, and flat parallel side walls.

II. COMPUTATIONAL METHOD

II.1. DISCRETIZATION METHOD

The steady, 2D Euler equations can be written on the domain $\Omega \subset \mathbb{R}^2$ as

$$\frac{\partial f(q)}{\partial x} + \frac{\partial g(q)}{\partial y} = 0, \quad \text{with} \tag{1}$$

$$q = \begin{pmatrix} \rho \\ \rho u \\ \rho v \\ \rho e \end{pmatrix}, \; f(q) = \begin{pmatrix} \rho u \\ \rho u^2 + p \\ \rho uv \\ \rho u(e + p/\rho) \end{pmatrix}, \; g(q) = \begin{pmatrix} \rho v \\ \rho uv \\ \rho v^2 + p \\ \rho v(e + p/\rho) \end{pmatrix}. \tag{2}$$

Here, q is the state vector of conservative quantities, and f and g are the so-called flux vectors. The primitive quantities used here are the density ρ, the velocity components u and v, and the pressure p. For a perfect gas, the total energy e is related to the primitive quantities as

$$e = \frac{1}{\gamma - 1}\frac{p}{\rho} + \frac{1}{2}(u^2 + v^2), \tag{3}$$

where γ is the ratio of specific heats.

To allow solutions with discontinuities, the Euler equations are discretized in the integral form

$$\int_{\partial\Omega^*} (f(q)\cos\phi + g(q)\sin\phi)ds = 0, \tag{4}$$

where Ω^* is an arbitrary subregion of Ω, $\partial\Omega^*$ the boundary of Ω^*, and $\cos\phi$ respectively $\sin\phi$ the x- and y-component of the outward unit normal on $\partial\Omega^*$. A straightforward and simple discretization of (4) is obtained by subdividing Ω into disjunct subregions $\Omega_{i,j}$ (the finite volumes), and by requiring that

$$\int_{\partial\Omega_{i,j}} (f(q)\cos\phi + g(q)\sin\phi)ds = 0 \tag{5}$$

for each finite volume separately.
Using the rotational invariance of the Euler equations:

$$f(q)\cos\phi + g(q)\sin\phi = T^{-1}(\phi)f(T(\phi)q), \tag{6}$$

where $T(\phi)$ is the rotation matrix

$$T(\phi) = \begin{pmatrix} 1 & 0 & 0 & 0 \\ 0 & \cos\phi & \sin\phi & 0 \\ 0 & -\sin\phi & \cos\phi & 0 \\ 0 & 0 & 0 & 1 \end{pmatrix}, \tag{7}$$

(5) can be rewritten as

$$\int_{\partial\Omega_{i,j}} T^{-1}(\phi)f(T(\phi)q)ds = 0. \tag{8}$$

As finite volumes we consider (arbitrarily shaped) quadrilaterals. The subdivision into quadrilaterals is such that $\Omega_{i\pm1,j}$ and $\Omega_{i,j\pm1}$ are the neighbouring volumes of $\Omega_{i,j}$ (Fig. 1a).
Crucial in the discretization is the evaluation of the flux vector along $\partial\Omega_{i,j}$. Along each finite volume wall separately we assume the flux vector to be constant, and we assume it to be determined by a uniformly constant left and right state only. Hence, (8) becomes

$$F_{i+\frac{1}{2},j} - F_{i-\frac{1}{2},j} + F_{i,j+\frac{1}{2}} - F_{i,j-\frac{1}{2}} = 0, \quad \text{with} \tag{9}$$

$$F_{i+\frac{1}{2},j} = T^{-1}(\phi_{i+\frac{1}{2},j})f(T(\phi_{i+\frac{1}{2},j})q^l_{i+\frac{1}{2},j}, T(\phi_{i+\frac{1}{2},j})q^r_{i+\frac{1}{2},j})l_{i+\frac{1}{2},j}, \tag{10}$$

and similar expressions for $F_{i-\frac{1}{2},j}$, $F_{i,j+\frac{1}{2}}$ and $F_{i,j-\frac{1}{2}}$. $F_{i+\frac{1}{2},j}$ represents the transport of mass, momentum and energy per unit of time across $\partial\Omega_{i+\frac{1}{2},j}$. In its expression, (10), $l_{i+\frac{1}{2},j}$ is the length of the finite volume wall $\partial\Omega_{i+\frac{1}{2},j}$, and the superscripts l and r refer to the left and right side of $\partial\Omega_{i+\frac{1}{2},j}$ respectively (Fig. 1b).
By considering the flux vector to be determined by a uniformly constant left and right state only, the actual flux evaluation is identical to the solution of a 1D Riemann problem. For this we use here a so-called approximate Riemann solver. Several approximate Riemann solvers exist [3, 4, 5, 6]. We have chosen Osher's Riemann solver because of: (i) its continuous differentiability, and (ii) its consistent treatment of boundary conditions [7, 8]. (The continuous differentiability guarantees the applicability of a Newton type solution technique, which is what we make use of.) Osher's scheme is generally said to be complicated and expensive compared to other approximate Riemann solvers. Arguments against this can be found in [8].
The approximate solution of the 1D Riemann problem is called the evolution stage of a so-called projection-evolution scheme [9]. Still to be filled in: the projection stage, i.e. the determination of the left and right states, such as $q^l_{i+\frac{1}{2},j}$ and $q^r_{i+\frac{1}{2},j}$ in (10). Depending on the way the states $q^l_{i+\frac{1}{2},j}$ and $q^r_{i+\frac{1}{2},j}$ are chosen, the discretization is first- or second-order accurate. First-order accuracy is simply obtained by taking

$$q^l_{i+\frac{1}{2},j} = q_{i,j}, \quad \text{and} \qquad q^r_{i+\frac{1}{2},j} = q_{i+1,j}. \tag{11}$$

Second-order accuracy can be obtained by for example the κ-schemes introduced by VAN LEER [9].
Two well-known drawbacks of the first-order accurate discretization are: (i) its need for relatively fine grids in smooth flow regions, and (ii) its strong smearing of discontinuities that are not aligned with the grid [10].

Second-order discretizations yield a strong improvement of both drawbacks. However, second-order discretized equations cannot be solved with the same good efficiency as first-order discretized equations [11]. Further, when using a second-order discretization, spurious non-monotonicity (wiggles) may arise at discontinuities [11].
Here, we prefer the first-order accurate discretization, since here: (i) the transonic shock will be well-aligned with the grid, and (ii) the best possible efficiency is preferred.

II.2. SOLUTION METHOD

II.2.1. RELAXATION METHOD

As a solution method for the first-order discretized equations we use: collective symmetric point Gauss-Seidel relaxation. *Point* refers to the fact that during the update of the state vector $q_{i,j}$ all other state vectors are kept fixed. *Collective* refers to the fact that the update of $q_{i,j}$ is done for all of its four components simultaneously. Further, *symmetric* means that after a relaxation sweep, i.e. after an update of all state vectors $q_{i,j}$, a new sweep in the reverse direction is made. At each volume visited during a relaxation sweep, we solve the four nonlinear equations (9) by Newton's method (local linearization). The most efficient relaxation is obtained by selecting a large tolerance for the Newton iteration so that in all but exceptional cases only a single Newton step is needed.

II.2.2. MULTIGRID METHOD

The solution method described so far is simple and robust, but needs an acceleration. With point Gauss-Seidel relaxation, a suitable acceleration technique is found in multigrid. As a very efficient and robust multigrid technique, we use: nonlinear multigrid preceded by nested iteration [8, 12]
Let

$$F_h(q_h) = 0 \tag{12}$$

denote the system of first-order discretized Euler equations. To apply multigrid we construct a nested set of grids, such that each volume on a coarse grid is the union of 2×2 volumes on the next finer grid (Fig. 2).
Let $\Omega_{h_1}, \Omega_{h_2}, \cdots, \Omega_{h_L}$ be a sequence of nested grids with Ω_{h_1} the coarsest and Ω_{h_L} the finest grid. Our multigrid solution of (12) can be divided into two successive stages. The first stage is nested iteration (or full multigrid) which is used to obtain a good initial solution on Ω_{h_L}. The second and last stage is nonlinear multigrid (or full approximation scheme) which is used to iterate until convergence. The first iterand for the nonlinear multigrid iteration is the solution obtained by nested iteration. We will now discuss these stages in more detail.

Nested iteration:
The nested iteration starts with a user-defined initial estimate of q_{h_1}; the solution on the coarsest grid. To obtain an initial solution on a finer grid $\Omega_{h_{l+1}}$, first the solution on the next coarser grid Ω_{h_l} is improved by a nonlinear multigrid cycle. Hereafter this solution is interpolated to the finer grid $\Omega_{h_{l+1}}$. These steps are repeated until the highest level (finest grid) has been reached. On a grid Ω_{h_l} with an even number of volumes in both the i- and j-direction, the interpolation used to obtain the initial solution on a next finer grid is bilinear. For this purpose the grid Ω_{h_l} is subdivided into disjunct sets of 2×2 volumes. The four state vectors corresponding with each set are interpolated in a bilinear way. Since each volume of Ω_{h_l} overlaps 2×2 volumes of $\Omega_{h_{l+1}}$, 4×4 new state vectors are obtained on $\Omega_{h_{l+1}}$. (On a coarsest grid with an uneven number of volumes in i- and/or j-direction, the interpolation used is linear.)

Nonlinear multigrid iteration:
A single nonlinear multigrid cycle is recurrently defined by the following steps:
(1) Improve on Ω_{h_l} the latest obtained solution q_{h_l} by application of p pre-relaxation sweeps.
(2) Compute on the next coarser grid $\Omega_{h_{l-1}}$ the righthand side $r_{h_{l-1}} = F_{h_{l-1}}(q_{h_{l-1}}) - I_{h_l}^{h_{l-1}} F_{h_l}(q_{h_l})$, where $I_{h_l}^{h_{l-1}}$ is a so-called restriction operator.
(3) Approximate the solution of $F_{h_{l-1}}(q_{h_{l-1}}) = r_{h_{l-1}}$ by the application of σ nonlinear multigrid cycles. Denote the approximation obtained as $\tilde{q}_{h_{l-1}}$.
(4) Correct the current solution by: $q_{h_l} = q_{h_l} + I_{h_{l-1}}^{h_l}(\tilde{q}_{h_{l-1}} - q_{h_{l-1}})$, where $I_{h_{l-1}}^{h_l}$ is a so-called prolongation operator.
(5) Improve again q_{h_l} by application of q post-relaxations.

Steps 2, 3 and 4 form the so-called coarse grid correction. (These three steps are skipped on the coarsest grid.) The efficiency of a coarse grid correction depends in general on the coarseness of the coarsest grid. (In general it holds: the coarser, the better.)
The restriction operator $I_{h_l}^{h_{l-1}}$ and the prolongation operator $I_{h_{l-1}}^{h_l}$ are defined by

$$(r_{h_{l-1}})_{i,j} = (I_{h_l}^{h_{l-1}} r_{h_l})_{i,j} \equiv (r_{h_l})_{2i,2j} + (r_{h_l})_{2i-1,2j} + (r_{h_l})_{2i,2j-1} + (r_{h_l})_{2i-1,2j-1}, \tag{13}$$

respectively

$$(I_{h_{l-1}}^{h_l} q_{h_{l-1}})_{2i,2j} = (I_{h_{l-1}}^{h_l} q_{h_{l-1}})_{2i-1,2j} = (I_{h_{l-1}}^{h_l} q_{h_{l-1}})_{2i,2j-1} = (I_{h_{l-1}}^{h_l} q_{h_{l-1}})_{2i-1,2j-1} \equiv (q_{h_{l-1}})_{i,j}. \tag{14}$$

Defining the transfer operators in this way, it can be verified that

$$F_{h_{l-1}} = I_{h_l}^{h_{l-1}} F_{h_l} I_{h_{l-1}}^{h_l}, \tag{15}$$

i.e. a coarse grid discretization of the Euler equations is a Galerkin approximation of the discretization on the next finer grid. This implies that the coarse grid correction reduces in an efficient way the low frequency components in the defect.
As values for σ, and p and q we generally use at each level separately: $\sigma = 1$, and $p = q = 1$; i.e. as nonlinear multigrid cycles we generally use V-cycles with one pre- and one post-relaxation.

In Fig. 3 an illustration is given of a complete solution process. A 5-level multigrid strategy has been considered. Between each pair AB, we have a nonlinear multigrid cycle (V-cycle). In the nested iteration stage, between each pair BA we have the bilinear prolongation of the solution.

III. GRID

III.1. GRID GENERATION

In Fig. 4 graphs are given of the wind tunnel section considered. In Fig. 4a a graph is given of the complete integration region. The graph shows a flat parallel inflow part, followed by a slender curved part up to the outlet. In Fig. 4b a photograph is given of the test section in an opened wind tunnel.

In order to obtain a good resolution of large local gradients (which were decided to be important), we used grids with local refinements; grids with stretching in both x- and y-direction. (Fig. 5).
The following stretching relations have been used for the x-coordinates of the vertical grid lines:

$$x_i = x_{shock} + (x_{in} - x_{shock}) \frac{e^{c_{x_1}(n_{x_1} - i)/n_{x_1}} - 1}{e^{c_{x_1}} - 1}, \quad i = 0, 1, \cdots, n_{x_1}, \quad \text{and}$$
$$x_i = x_{shock} + (x_{out} - x_{shock}) \frac{e^{c_{x_2}(i - n_{x_1})/n_{x_2}} - 1}{e^{c_{x_2}} - 1}, \quad i = n_{x_1}+1, n_{x_1}+2, \cdots, n_{x_1}+n_{x_2}. \tag{16}$$

Here, the subscript *shock* refers to a vertical grid line which is supposed to lie in the foot of the shock wave. The subscripts *in* and *out* refer to the vertical grid line at the in- and outlet respectively. The (positive) constants c_{x_1} and c_{x_2} determine the stretching up- and downstream of x_{shock} respectively. The larger the constants, the higher the stretching. Further, the numbers n_{x_1} and n_{x_2} denote the number of volumes in x-direction, up- and downstream of x_{shock} respectively. For the y-coordinates of the volume vertices the following stretching relation has been used:

$$y_j(x) = y_{low}(x) + (y_{up}(x) - y_{low}(x)) \frac{e^{c_y j/n_y} - 1}{e^{c_y} - 1}, \quad j = 0, 1, \cdots, n_y. \tag{17}$$

Here the subscripts *low* and *up* refer to the lower and upper wall respectively. The (positive) constant c_y determines the stretching in y-direction, the number n_y denotes the total number of volumes in y-direction. The y-distribution of the lower and upper wall, $y_{low}(x)$ and $y_{up}(x)$, are known from accurate measurements at discrete x-positions in the real test section. At intermediate x-positions, we used cubic spline interpolation.

Smoothness requirements that we imposed on (16) and (17) are:

$$\frac{x_i - x_{i-1}}{x_{i+1} - x_i} \leqslant 1 + \delta, \quad i = 0, 1, \cdots, n_{x_1},$$
$$\frac{x_{i+1} - x_i}{x_i - x_{i-1}} \leqslant 1 + \delta, \quad i = n_{x_1}+1, n_{x_1}+2, \cdots, n_{x_1}+n_{x_2}, \tag{18}$$

and

$$\frac{y_{j+1}(x)-y_j(x)}{y_j(x)-y_{j-1}(x)} \leq 1+\delta, \quad j=0,1,\cdots,n_y, \quad x_{in} \leq x \leq x_{out}. \tag{19}$$

Assuming that $c_{x_1}/n_{x_1} \ll 1$, $c_{x_2}/n_{x_2} \ll 1$ and $c_y/n_y \ll 1$, above requirements can be rewritten by good approximation as

$$\begin{aligned} c_{x_1}/n_{x_1} &\leq \frac{\delta}{1+\delta}, \quad & x \leq x_{shock}, \\ c_{x_2}/n_{x_2} &\leq \delta, \quad & x > x_{shock}, \end{aligned} \tag{20}$$

and

$$c_y/n_y \leq \delta. \tag{21}$$

So: the coarser the grid, the stronger the constraint on the stretching parameters c_{x_1}, c_{x_2} and c_y. The smoothness requirements (20) and (21) have been imposed now for the coarsest grid only. As a value for δ has been chosen: $\delta = 1$.
Further, for the finest grid only we imposed the following matching requirement:

$$\frac{x_{i+1}-x_i}{x_i-x_{i-1}} = 1, \quad x_i = x_{shock}. \tag{22}$$

III.2. GRID ADAPTATION

The value of x_{shock} has not been chosen but has been initialized to the x-location of the wind tunnel throat, and has been adapted to the shock location during the nested iteration stage. The grid adaptation is simple. First, after each solution prolongation in the nested iteration stage, a search is made for the x-location of the maximum velocity gradient at the lower wall, downstream of the throat. This location is assigned to x_{shock}. Hereafter, we generate the new grids. Without any correction, the states $q_{i,j}$ are shifted together with the volumes $\Omega_{i,j}$. Doing this, the quality of the finest grid solution as yielded by the nested iteration becomes worse. However, no significant deterioration of convergence rates has been observed.

IV. BOUNDARY CONDITIONS

IV.1. DIFFERENT BOUNDARY CONDITIONS CONSIDERED

The boundary condition treatment must be correct both mathematically and physically. Mathematics prescribes how many conditions must be imposed at a boundary, physics prescribes what conditions should be imposed.

The number of conditions to be imposed at a boundary depends on the type of flow at that boundary. Types of flows to be considered here, and the corresponding number of boundary conditions to be imposed are: (i) subsonic inflow (three), (ii) subsonic outflow (one), and (iii) impermeable walls (one). The following conditions have been imposed.

Upper and lower wall:
At the impermeable upper and lower wall, the boundary condition imposed is trivial: a zero normal velocity component.

Inlet:
Uniformly constant distributions $u = u_{in}$, $v = 0$ and $c = 1$, with c denoting the speed of sound, have been imposed. These distributions are motivated by the fact that the inlet part is flat and parallel. As a subsonic value for u_{in} has been taken: the 1D flow theory value, given a sonic throat.

Outlet:
Because of the fact that the outlet part is non-flat and non-parallel, the outlet boundary condition cannot be as trivial as those at the inlet. The following possibilities have been considered: (i) $h = h_{in}$ is uniformly constant, with h denoting the total enthalpy: $h = c^2/(\gamma-1) + \frac{1}{2}(u^2+v^2)$, (ii) $v/u = \theta(y)$, (iii) $u = u(y)$, and (iv) $p = p(y)$.

The *first* possibility was motivated by the fact that with a known uniformly constant distribution of u, v and c at the inlet (i.e. with a known uniformly constant total enthalpy at the inlet), this boundary condition requires no knowledge of the non-uniform outlet flow. This because of the fact that for steady, 2D Euler flows, with at the upstream boundary the total enthalpy known to be constant, only three differential equations describe the flow. The energy equation in its differential form may be replaced by the relation $c^2/(\gamma-1)+½(u^2+v^2)=h_{in}$ throughout the entire flow field. The present Euler code solves the full non-isenthalpic Euler equations. To allow the computation of non-isenthalpic Euler flows such as the flow through a propeller disk [13], and in particular to allow a rapid extension to a Navier-Stokes code [14], the simplifying property mentioned has not been exploited.

The *second* possibility, with the flow direction specified, was motivated by its simplicity. A linear distribution of $\theta(y)$ has been assumed, using the known flow direction at the lower and upper wall.

The *third* possibility was also motivated by its simplicity. For this possibility, we assumed the outlet flow to be a potential vortex flow. The relation $u(y)r(y)=\psi_{out}$ has been applied, with ψ_{out} uniformly constant and $r(y)$ the distribution of the radii of curvature of the streamlines. A linear distribution for the streamline curvature $1/r(y)$ has been assumed, using the known curvature of the lower and upper wall. As a value for ψ_{out} has been taken: a value close to the value following from the 1D flow theory, given a sonic throat with a fully subsonic flow further downstream. A disadvantage of this boundary condition is its inconsistency in the case of a flow with shock wave of variable strength, which is what we have here. (It is a boundary condition which is always consistent in a potential flow model, but not in the Eulerian rotational flow model.)

For the *fourth* possibility we used the equation of curvilinear motion

$$\frac{dp(y)}{dy} = \gamma\frac{p(y)M^2(y)}{r(y)}\cos\phi(y), \tag{23}$$

with $M(y)$ the Mach number distribution and $\phi(y)$ the distribution of the angles between the streamlines and the x-axis. $M(y)$ has been taken uniformly constant. Its value has been determined with the 1D flow theory, given again a sonic throat and a fully subsonic flow downstream. For $1/r(y)$ and $\phi(y)$ again linear distributions have been assumed, such that the flow fits the channel outlet. A value close to the 1D flow theory value (given again a sonic throat with a fully subsonic outflow) has been used as a value for $p(x_{out}, y_{low})$. This yielded an initial value problem which has been solved by means of a Runge-Kutta-Merson method.

IV.2. WELL-POSEDNESS OUTLET BOUNDARY CONDITIONS

Generally speaking, mathematically well-posed conditions to be imposed at a boundary are: conditions for which the state at that boundary can be completed accurately. At an outlet, the boundary condition must fix the single degree of freedom existing overthere. An outlet boundary condition can be represented as a 3D surface in a 4D state space. The smaller the angle α between the normal at this surface and the eigenvector corresponding with the negative eigenvalue of the Jacobian: $u-c$, the better the quality of the outlet boundary condition. Considering the (ρ,u,v,e)-space as state space, the eigenvector corresponding with the eigenvalue $u-c$ is: $r=(\rho,-c,0,c(c/\gamma-u))^T$. For respectively h, v/u, u and p specified, the 3D surface mentioned, say $B(q)$, is described by

$$B(q) = \gamma e-\frac{\gamma-1}{2}(u^2+v^2)=h_B, \tag{24a}$$

$$B(q) = v/u=\theta_B, \tag{24b}$$

$$B(q) = u=u_B, \quad \text{and} \tag{24c}$$

$$B(q) = (\gamma-1)\rho(e-\tfrac{1}{2}(u^2+v^2))=p_B, \tag{24d}$$

with h_B, θ_B, u_B and p_B constant. For the angle α it holds that $\cos\alpha\propto\nabla B.r$, with $\nabla=(\partial/\partial\rho,\ \partial/\partial u,\ \partial/\partial v,\ \partial/\partial e)^T$. For respectively h, v/u, u and p specified we find

$$\nabla B.r = c(c-u), \tag{25a}$$

$$\nabla B.r = -(v/u)(c/u), \tag{25b}$$

$$\nabla B.r = -c, \quad \text{and} \tag{25c}$$

$$\nabla B.r = \gamma p. \tag{25d}$$

From (25a) and (25b) it can be seen that for h and v/u specified, the vectors ∇B and r become orthogonal for $u \to c$ respectively $v \to 0$. The consequence of a nearly orthogonal ∇B and r is that a small change in either the boundary condition or the state inside the integration region near the outlet, may cause a large change in the boundary state and hence in the flux across the outlet. For a given state $q_0=(u_0,\ v_0,\ c_0,\ z_0)^T$ near the outlet, with $z_0=\ln(p_0\rho_0^{-\gamma})$, and the boundary conditions specified by (24a)-(24d) respectively, the effect of a perturbation in q_0 will be shown.

The state at the outlet is $q=(u,\ v_0,\ c,\ z_0)^T$, with for boundary condition (24a)-(24d) respectively

$$c = \frac{\gamma-1}{\gamma+1}(u_0+\frac{2}{\gamma-1}c_0+\sqrt{(\gamma+1)(h_B-\frac{1}{2}v_0^2)-\frac{\gamma-1}{2}(u_0+\frac{2}{\gamma-1}c_0)^2}), \tag{26a}$$

$$u = v_0/\theta_B, \tag{26b}$$

$$u = u_B, \tag{26c}$$

$$c = \sqrt{\gamma p_B^{(\gamma-1)/\gamma}e^{z_0/\gamma}}, \tag{26d}$$

and either $u=u_0+\frac{2}{\gamma-1}(c_0-c)$ or $c=c_0+\frac{\gamma-1}{2}(u_0-u)$ to complete.
With $\nabla=(\partial/\partial u_0,\ \partial/\partial v_0,\ \partial/\partial c_0,\ \partial/\partial z_0)^T$ we find for (26a)-(26d) respectively

$$\nabla c = \frac{\gamma-1}{\gamma+1}(1,0,\frac{2}{\gamma+1},0)^T-\frac{\gamma-1}{\gamma+1}\frac{1}{c-u}(\frac{\gamma-1}{2}u+c,\ \frac{\gamma+1}{2}v,\ u+\frac{2}{\gamma-1}c,0)^T, \tag{27a}$$

$$\nabla u = (0,u/v,0,0)^T, \tag{27b}$$

$$\nabla u = 0, \quad \text{and} \tag{27c}$$

$$\nabla c = (0,0,0,c/2\gamma)^T, \tag{27d}$$

where we substituted $q=q_0$ into (27a) and (27b) for simplicity. It can be seen that the gradient pairs (27a) and (27b) become infinitely large in aforementioned limit cases ($u\to c$ for h specified and $v\to 0$ for v/u specified). Flow computations with h specified and v/u specified showed these outlet boundary conditions to be ill-posed indeed. This was not the case with the two other boundary conditions.

Because of its better consistency with the Euler flow model, the boundary condition with p specified has been preferred above the boundary condition with u specified.

V. RESULTS

V.1. COMPUTATIONAL RESULTS

The large slenderness of the wind tunnel section led to a coarsest grid with a relatively large number of volumes in longitudinal direction. By using a 56×8-grid as finest grid and a 4-level multigrid strategy, a 7×1-grid became the coarsest grid (Fig. 6). (The dashed lines in Fig. 6 indicate the lower and upper wall of the wind tunnel section.)
As a consequence of this relatively fine coarsest grid, the number of nonlinear multigrid cycles required was somewhat larger than the few cycles which are supposed to be necessary when having optimal multigrid efficiency. To slightly improve the multigrid convergence properties we increased the number of pre- and post-relaxations performed on the coarsest grid.

As flow problems we considered a non-choked flow with $M_u=1.15$, M_u being the Mach number just upstream of the shock wave, and a choked flow with $M_u=1.37$.
Convergence histories obtained for both test cases are given in Fig. 7. The convergence histories are given by graphs of the residual ratio $\Sigma_{i=1}^4|r_h^n(i)|_{max}/\Sigma_{i=1}^4|r_h^1(i)|_{max}$ versus the number of nonlinear multigrid cycles performed. Here, $|r_h^n(i)|_{max}$ denotes the maximum absolute value over all volumes, of the i-th component of the residual $r_h^n=F_h(q_h^n)$, and n denotes the n-th cycle in the nonlinear multigrid iteration. The less good convergence rate obtained for the choked flow might be related to the fact that for this flow the subsonic flow upstream of the supersonic region does not feel the outlet pressure specified.
Finest grids and surface distributions obtained for $M_u=1.15$ and $M_u=1.37$ are shown in Fig. 8a and 8b respectively. The markers in the surface distributions correspond to volume wall centres; the square to those at the lower surface and the circular to those at the upper surface. From the finest grids and surface distributions obtained, it can be seen that for both flows the grid adaptation is good. Clearly visible for $M_u=1.37$ is the occurrence of an after-expansion. Since a first-order accurate Osher-type discretization yields solutions without spurious non-monotonicity, the after-expansion occurring for $M_u=1.37$ is not a numerical artefact, but a correct part of the Euler flow solution indeed.

V.2. COMPARISON WITH HOLOGRAPHIC INTERFEROMETRY RESULTS

For both the choked and non-choked flow a comparison is made between the Mach number distributions obtained with the Euler code and those obtained by holographic interferometry.
In Fig. 9 the Mach number distributions are given as obtained for the entire test section. In Fig. 10 a detail of both distributions is compared with the corresponding interferometrical result. It appears

that the computational and interferometrical results show a perfect quantitative agreement away (of course) from the wall and shock wave.
The differences between both results can be exploited. Given an Euler code which has proved to be reliable, its results can be considered confidently as experimental results with viscosity and heat conduction switched off. Its results can be used to pick out from experimental results: simple viscous phenomena and, in particular, complicated viscous-inviscid phenomena. The present Euler code has proved to be reliable [11, 13, 15]. Here, its results learn us for instance that the supersonic after-expansion (at both $M_u = 1.15$ and $M_u = 1.37$) and the λ-shock (at $M_u = 1.37$) are viscous-inviscid phenomena indeed, and further that due to viscous effects the shock wave has been pushed slightly upstream (at both $M_u = 1.15$ and $M_u = 1.37$).

VI. CONCLUSIONS

For the steady, 2D, non-isenthalpic Euler equations, an outlet boundary condition with total enthalpy or flow direction specified yields a mathematically ill-posed problem, whereas an outlet boundary condition with static pressure specified yields a mathematically well-posed problem.
The convergence rates obtained are not optimal seen from the viewpoint of multigrid techniques, though still very good seen from the viewpoint of almost any other solution technique. The multigrid convergence behaviour suffered somewhat from the relatively large number of volumes in streamwise direction on the coarsest grid.
Non-oscillatory solutions with sharp shocks have been obtained. Automatic grid adaptation during the nested iteration works well. Away from walls and shock wave, the agreement between computational and experimental results is good.
The utility of a reliable Euler code in research on viscous-inviscid interactions may be twofold. It may be used: (i) as a tool for designing (and re-designing) an experimental set-up, and (ii) as a tool for understanding complicated experimental results. The latter use does not seem to be important in present-day research. However, given the recent availability of very reliable (and moreover very efficient) Euler codes, this use might become of paramount importance in near-future research.

REFERENCES

1. C. NEBBELING and W.J. BANNINK (1984). *A Curved Test Section for Research on Transonic Shock Wave - Boundary Layer Interaction.* Delft University of Technology, Delft, Report LR-414.
2. C. NEBBELING and B. KOREN (1987). *An Experimental-Computational Investigation of Transonic Shock Wave - Turbulent Boundary Layer Interaction in a Curved Test Section.* Centre for Mathematics and Computer Science, Amsterdam, Report NM-R8716.
3. J.L. STEGER and R.F. WARMING (1981). Flux-Vector Splitting of the Inviscid Gas Dynamic Equations with Applications to Finite-Difference Methods. *J. Comput. Phys. 40,* 263-293.
4. B. VAN LEER (1982). Flux-Vector Splitting for the Euler Equations. *Proceedings of the 8th International Conference on Numerical Methods in Fluid Dynamics,* Aachen, 1982. Lecture Notes in Physics 170, 507-512, Springer, Berlin.
5. P.L. ROE (1981). Approximate Riemann Solvers, Parameters Vectors, and Difference Schemes. *J. Comput. Phys. 43,* 357-372.
6. S. OSHER and F. SOLOMON (1982). Upwind Difference Schemes for Hyperbolic Systems of Conservation Laws. *Math. Comp. 38,* 339-374.
7. S. OSHER and S. CHAKRAVARTHY (1983). Upwind Schemes and Boundary Conditions with Applications to Euler Equations in General Geometries. *J. Comput. Phys. 50,* 447-481.
8. P.W. HEMKER and S.P. SPEKREIJSE (1986). Multiple Grid and Osher's Scheme for the Efficient Solution of the Steady Euler Equations. *Appl. Num. Math. 2,* 475-493.
9. B. VAN LEER (1985). Upwind-Difference Methods for Aerodynamic Problems governed by the Euler Equations. *Proceedings of the 15th AMS-SIAM Summer Seminar on Applied Mathematics,* Scripps Institution of Oceanography, 1983. Lectures in Applied Mathematics 22, 327-336, AMS, Providence, Rhode Island.
10. P.W. HEMKER (1986). Defect Correction and Higher Order Schemes for the Multi Grid Solution of the Steady Euler Equations. *Proceedings of the 2nd European Conference on Multigrid Methods,* Cologne, 1985, Lecture Notes in Mathematics 1228, 150-165, Springer, Berlin.
11. B. KOREN (1987). Defect Correction and Multigrid for an Efficient and Accurate Computation of Airfoil Flows. *To appear in J. Comput. Phys.*
12. W. HACKBUSCH (1985). *Multi-Grid Methods and Applications,* Springer, Berlin.

13. B. KOREN and S.P. SPEKREIJSE (1987). Multigrid and Defect Correction for the Efficient Solution of the Steady Euler Equations. *Proceedings of the 25th Meeting of the Dutch Association for Numerical Fluid Mechanics*, Delft, 1986. Notes on Numerical Fluid Mechanics 17, 87-100, Vieweg, Braunschweig.
14. B. KOREN (1987). *First-Order Upwind Schemes and Multigrid for the Steady Navier-Stokes Equations.* Centre for Mathematics and Computer Science, Amsterdam, Report NM-R87XX.
15. P.W. HEMKER and B. KOREN (1987). A Non-linear Multigrid Method for the Steady Euler Equations. *To appear in Proceedings GAMM-Workshop on the Numerical Solution of Compressible Euler Flows*, Rocquencourt, 1986. Notes on Numerical Fluid Mechanics XX. Vieweg, Braunschweig.

FIGURES

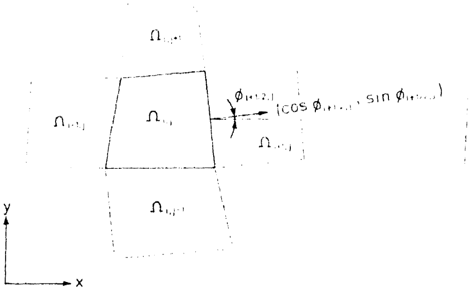

a. Geometry.

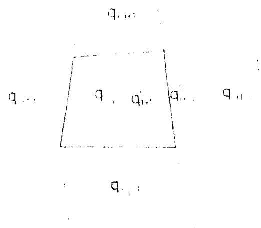

b. State vectors.

Fig. 1. Finite volume $\Omega_{i,j}$.

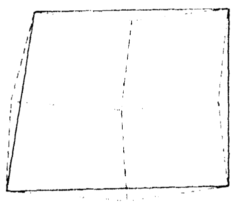

Fig. 2. Coarse grid volume and corresponding fine grid volumes.

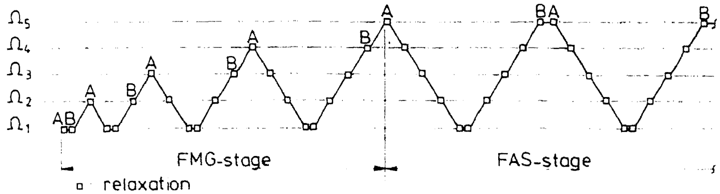

Fig. 3. Schematic representation of a (5-level) multigrid strategy.

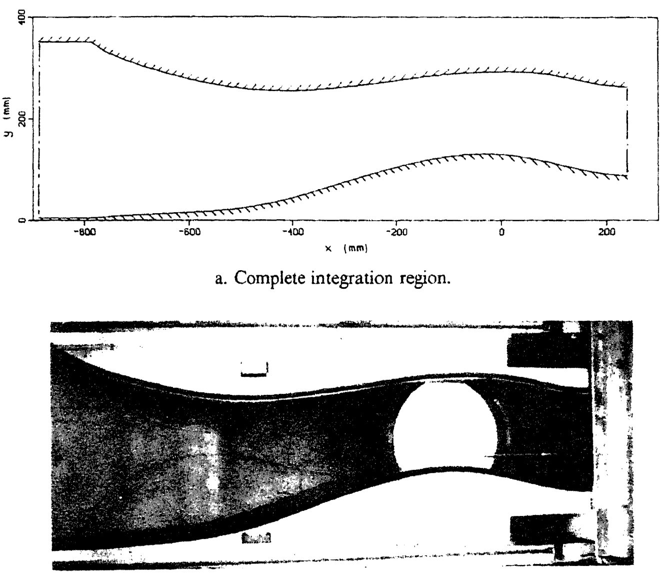

a. Complete integration region.

b. Test section in opened wind tunnel.

Fig. 4. Wind tunnel section.

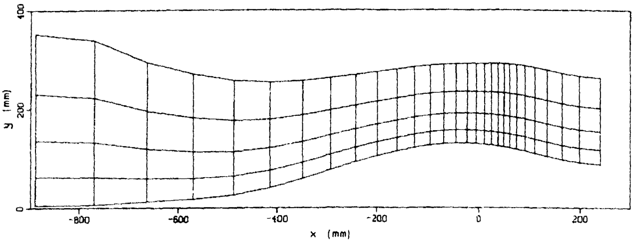

Fig. 5. Stretched grid.

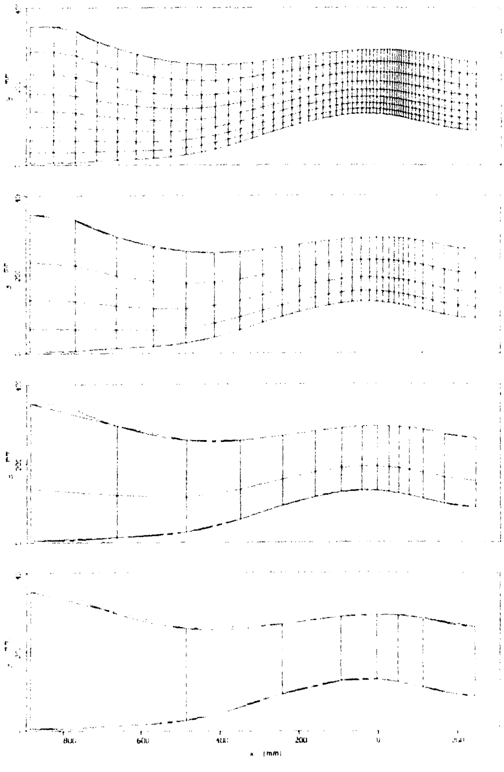

a. 56×8-grid.

b. 28×4-grid.

c. 14×2-grid.

d. 7×1-grid.

Fig. 6. Family of grids.

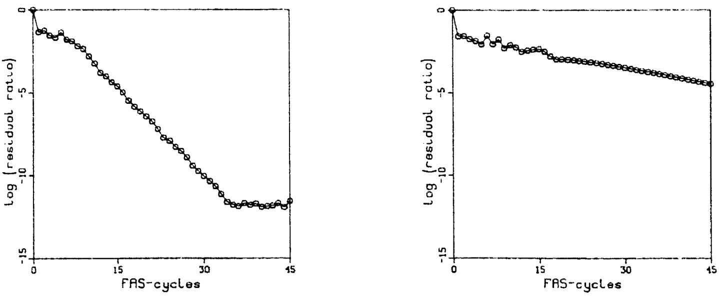

a. $M_u = 1.15$.   b. $M_u = 1.37$.

Fig. 7. Convergence histories.

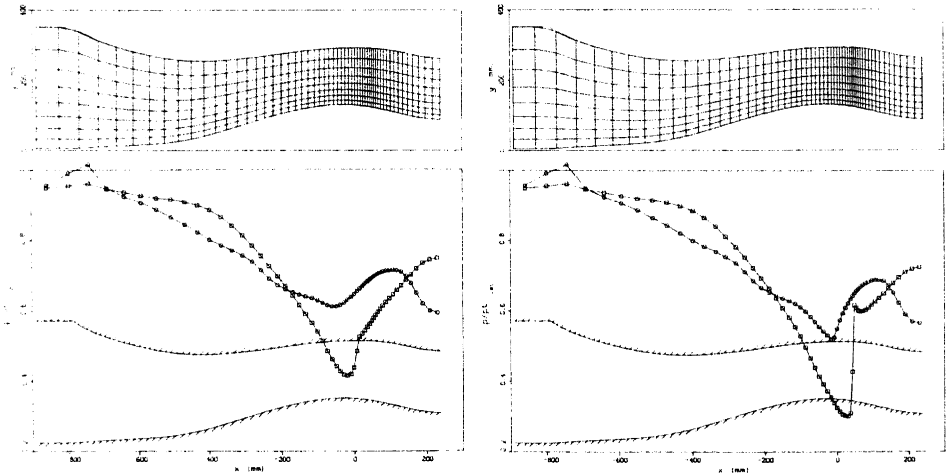

a. $M_u = 1.15$.   b. $M_u = 1.37$.

Fig. 8. Grids and surface distributions.

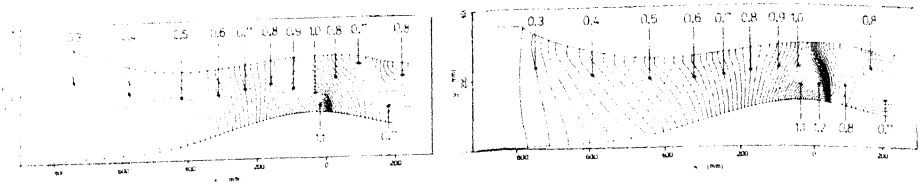

a. $M_u = 1.15$. b. $M_u = 1.37$.

Fig. 9. Mach number distributions.

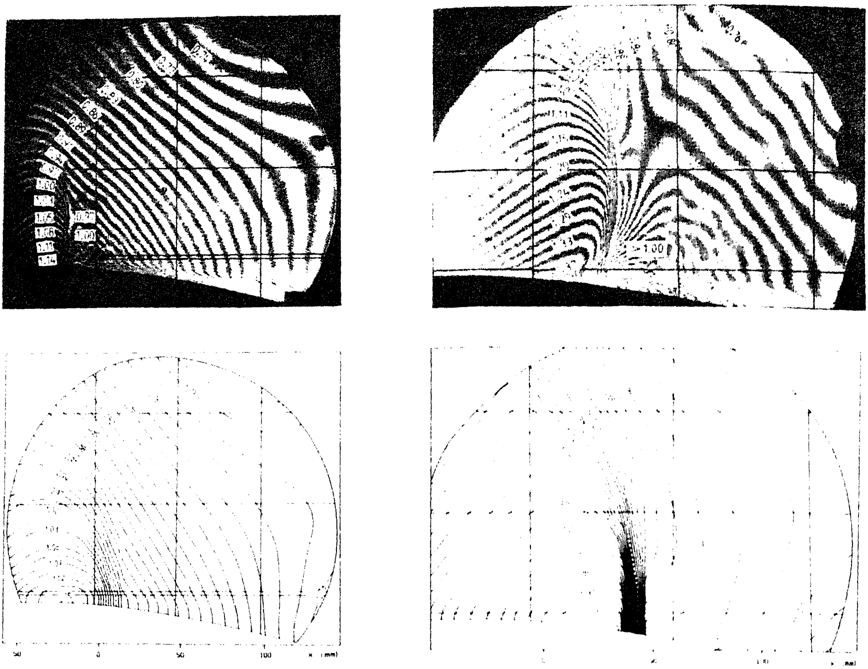

a. $M_u = 1.15$. b. $M_u = 1.37$.

Fig. 10. Interferometrical and numerical Mach number distributions.